Identification of Ni-vacancy defect in Ni-Mn-Z (Z = Ga, Sn, In): An experimental and DFT positron annihilation study

I. Unzueta,[1,2,*] V. Sánchez-Alarcos,[3,4,†] V. Recarte,[3,4,‡] J. I. Pérez-Landazábal,[3,4,§] N. Zabala,[1,5,¶] J. A. García,[6,2,**] and F. Plazaola[1,††]

[1] *Department of Electricity and Electronics, University of the Basque Country UPV/EHU, 48940 Leioa, Spain*
[2] *BCMaterials, University of Basque Country UPV/EHU, 48940 Leioa, Spain*
[3] *Department of Science, Universidad Pública de Navarra, Campus de Arrosadía, 31006 Pamplona, Spain*
[4] *Institute for Advanced Materials (INAMAT), Universidad Pública de Navarra, Campus de Arrosadía, 31006 Pamplona, Spain*
[5] *Materials Physics Center (CSIC-UPV/EHU) and Donostia International Physics Center (DIPC), Paseo Manuel de Lardizabal 5, 20018 Donostia-San Sebastián, Spain*
[6] *Department of Applied Physics II, University of the Basque Country UPV/EHU, 48940 Leioa, Spain*

By means of experimental positron annihilation lifetime measurements and theoretical DFT positron lifetime calculations, vacancy type defects in $Ni_{50}Mn_{50-x}Sn_x$ (x = 25, 20, 15, 13, 10) and $Ni_{50}Mn_{50-x}In_x$ (x = 25, 20, 16, 13) systems are systematically studied. The study is extended to Ni-Mn-Ga systems as well. Experimental results are complemented with electron-positron DFT calculations carried out within LDA and GGA, where five different parameterizations accounting the $\gamma(\mathbf{r})$ enhancement factor are analyzed. Theoretical results indicate that the Boronski-Nieminen parameterization of $\gamma(\mathbf{r})$ is the one that best predicts the experimental results, which ultimately enables to identifiy V_{Ni} as the vacancy present in the studied samples. The characteristic positron lifetime related to V_{Ni} ranges between 181 - 191 ps in Ni-Mn-Sn/In systems. PALS results in these two systems delimit the lower bound of the achievable vacancy concentration, which is much larger comparing with the reported values in Ni-Mn-Ga systems. The present work, along with setting the basis for positron simulations in Ni-Mn based Heusler alloys, delimits the effect that the variation of vacancies have in the martensitic transformation in Ni-Mn-Sn systems.

I. INTRODUCTION

The multifunctional properties that Ni-Mn-Z (Z = Ga, In, Sn, Sb) Heusler alloys exhibit, such as giant magnetoresistance[1,2], magnetocaloric effect[3,4], large magnetic field induced strain[5,6] and shape-memory effect[7], are directly related with the occurrence of the so-called martensitic transformation (MT). MT is a displacive phase transition which occurs between highly symmetric austenitic phase and less symmetric martensitic structure[8]. Due to the magnetosctructural coupling these alloys exhibit, the structural transition is often accompanied with a magnetic transition. In Ni-Mn based Heusler alloys, the magnetism is mainly based on the indirect exchange between Mn atoms and the magnetic properties depend strongly on Mn-Mn distance[9]. Thus, whereas in the case of Ni-Mn-Ga systems the MT occurs between similar ferromagnetic parent and martensite phases[10], in the so-called metamagnetic shape memory alloys, Ni-Mn-Z (Z = In, Sn, Sb), the MT often takes place between a ferromagnetic austenite and a weak magnetic or paramagnetic martensite[7]. This magnetization discrepancy ΔM between parent and martensite phases gives rise to additional multifunctional effects such as the inverse magnetic field induced shape-change[11] and the inverse magnetocaloric effect[12,13].

All in all, the control of the MT plays a key role on the tuning of the aforementioned multifunctional properties. On the one hand, it is well known that the composition is the most critical factor affecting the MT temperature (T_{MT})[7,14–16]. In addition to composition, recent works have shown that the control of the microstructure becomes crucial to properly tune the MT and the related multifunctional properties[17–19]. Indeed, in Ni-Mn-Sn systems, the retained internal strain at anti-phase boundaries promotes the antiferromagnetic coupling between Mn atoms, affecting the magnetostructural properties and ultimately the width of MT[20]. In addition, the variation of the atomic order has profound effects on the transition temperature, enabling shifts of T_{MT} up to $\Delta T_{MT} \approx 100$ K[21]. On the other hand, the presence of defects alters the ferromagnetic interactions[18,22], and in the micro and nano regime, they may inhibit the MT[23].

In that connection, several works have already suggested the potential role that vacancies may play on the MT and the magnetic properties of Ni based Heusler Alloys. Zhang *et al.*[26] suggest that the observed magnetic entropy change in Ni-Mn-Sn ribbons may be a consequence of the enhancement of the atomic order which may be due to the annealing of vacancies. Moreover, Zhenni *et al.*[27] and Kustov *et al.*[28,29] point out the potential role that vacancy defects could have on the pinning of the MT, whereas Sánchez-Alarcos *et al.*[30] and

Initial Characterization parameters				Crystallographic Data		
Composition	Label	T_{MT} (K)	T_c (K)	Lattice Parameters (Å)	Simulated Phase	Ref.
$Ni_{50}Mn_{25}Sn_{25}$	Sn_{25}	(—)	328	$a = b = c = 6.046$	$Fm\bar{3}m$	[14]
$Ni_{50}Mn_{30}Sn_{20}$	Sn_{20}	(—)	343	$a = b = c = 6.024$	$Fm\bar{3}m$	[14]
$Ni_{50}Mn_{35}Sn_{15}$	Sn_{15}	223	313	$a = b = c = 5.995$	$Fm\bar{3}m$	[14]
$Ni_{50}Mn_{37}Sn_{13}$	Sn_{13}	310	$\approx T_{MT}$	$a = 4.317$ $b = 5.621$ $c = 4.361$	Pmma	[24]
$Ni_{50}Mn_{40}Sn_{10}$	Sn_{10}	473	(—)	$a = 4.333$ $b = 5.570$ $c = 4.281$	P2/m	[14]
$Ni_{50}Mn_{25}In_{25}$	In_{25}	(—)	310	$a = b = c = 6.071$	$Fm\bar{3}m$	[15]
$Ni_{50}Mn_{30}In_{20}$	In_{20}	(—)	298	$a = b = c = 6.031$	$Fm\bar{3}m$	[15]
$Ni_{50}Mn_{34}In_{16}$	In_{16}	225	300	$a = b = c = 6.004$	$Fm\bar{3}m$	[15]
$Ni_{50}Mn_{37}In_{13}$	In_{13}	393	$\approx T_{MT}$	$a = 4.391$ $b = 5.620$ $c = 4.331$	P2/m	[25]
$Ni_{50}Mn_{40}In_{10}$	In_{10}	(—)	(—)	$a = 4.284$ $b = 5.811$ $c = 4.301$	P2/m	[15 and 25]

Table I. Composition and characteristic T_{MT} and T_c temperatures obtained from the initial characterization measurements of the studied samples. Crystallographic data employed in AT-SUP calculations of the studied for $Ni_{50}Mn_{50-x}Sn_x$ (x = 25, 20, 15, 13, 10) and $Ni_{50}Mn_{50-x}In_x$ (x = 25, 20, 16, 13, 10) samples.

Santamarta *et al.*[31] suggest different vacancy dynamics as a responsible of the observed changes on Curie's temperature T_c and T_{MT} in Ni-Mn-Ga and Ni-Fe-Ga alloys, respectively. In a recent work Hedayati *et al.*[32] claim that Sn vacancies in Ni-Mn-Sn systems can be used to obtain shifts on T_{MT} up to 80 K. However, none of the previous works contribute any experimental evidence on vacancies.

Thus far, the vast majority of works focused on the effect of vacancies in MT and magnetic properties of Ni-based Heusler alloys have been conducted within the theoretical framework. For instance, from first principles calculations, Bai *et al.*[33–35] and Kulkova *et al.*[36,37] calculated the formation energy of possible anti-site and vacancy defects on several Ni-based Heusler compounds. In recent works, by first principles calculations and Monte Carlo simulations, Kosogor *et al.*[38] and Wang *et al.*[39], respectively, link the vacancy concentration (C_v) with the ordering process and the effect on the shift of the T_{MT}. In this context, Tehrani *et al.*[40], by means of molecular dynamics simulations also suggest the potential effect that vacancies may have on T_{MT}. Despite of the amount of investigations suggesting the non-trivial role that vacancies may play on the MT, experimental works have been scarcely reported, being the elusive nature of the vacancies' effect the reason making it less investigated comparing with other physical factors.

One of the most thorough study has been performed by Merida *et al.*[41–44]. By Positron Annihilation Lifetime Spectroscopy (PALS) they experimentally measure the C_v present in Ni-Mn-Ga single- and poly-crystals. Depending on the composition, they report different equilibrium vacancy concentration, as well as different migration and formation energies of vacancies. Additionally, they show that with proper annealing treatments[42], C_v can be tuned from $\approx$ 2000 ppm down to 10 ppm. These works demonstrate the capability of PALS for the study of vacancy dynamics in Ni-based Heusler Alloys. In fact, this technique has been widely used over decades and it is a powerful tool for defect characterization in metals[45]. As the positron lifetime is directly related with the electronic density of the material, crystal imperfections such as vacancy defects, alter significantly the surrounding electronic density. Thus, when positrons are trapped in such defects the positron lifetime varies, enabling a direct detection of vacancies.

In this work, vacancy-type defects are systematically investigated by PALS in Ni-Mn-In and Ni-Mn-Sn systems. The experimental measurements are complemented with Density Functional Theory (DFT) calculations of the positron lifetime. In order to establish the parameterization of the enhancement factor which best suits the experimental PALS results in Ni-Mn based Heusler alloys, a widely used five different parameterizations have been also comparatively studied. Results show that the Boronski-Nieminen parameterization gives the most accurate values for positron lifetimes, which, in turn, enables the identification of Ni vacancy (V_{Ni}) as the vacancy type present in the Ni-Mn-Sn, Ni-Mn-In and Ni-Mn-Ga systems. Taking advantage of the existing PALS results on Ni-Mn-Ga, theoretical calculations have been carried out in Ni-Mn-Ga to test the agreement between calculations and experimental results. Finally, and contrary to what happens in Ni-Mn-Ga systems, results in Ni-Mn-Sn and in Ni-Mn-In systems show that the irreducible high C_v, presents a handicap for its control by means of standard heat treatments.

II. EXPERIMENTAL METHOD

$Ni_{50}Mn_{50-x}Sn_x$ (x = 25, 20, 15, 13, 10) and $Ni_{50}Mn_{50-x}In_x$ (x = 25, 20, 16, 13) (Sn_x and In_x respectively) polycrystalline ingots are synthesized from high purity elements by arc melting method under protective argon atmosphere. Each initial ingot is remelted up to eight times to ensure the homogeneity. Afterwards, Sn_x and In_x samples are homogenized at 1173 K during 24 h. Regarding Sn_x samples, a further annealing of 4 h at 1273 K is performed to avoid dendritic structures[46]. Bulk pieces for the initial characterization are obtained from the center of each ingot by cutting small pieces using a low speed diamond saw. The initial characterization consists in EDX analysis and differential scanning calorimetric measurements (DSC) carried out in a TA Q100 DSC, by which the composition and the characteristic T_{MT} and Curie's T_c temperatures are determined. The results of the initial characterization are gathered in Table I (the compositional error obtained for all samples lay within 1.5% of the nominal composition), which are consistent with previous experimental reports[14,15].

Subsequently, Sn_x and In_x samples are quenched from 1173 K into iced water (AQ state). In order to ensure thermal equilibrium, samples are kept at 1173 K during 30 min before quenching. The study of the microstructural evolution of the vacancy defects upon post quenching has been performed using the approach employed in Ref. [41]. The samples are subjected to the so-called isochronal annealing cycles (IAC). In essence, the sample is heated up at a constant rate of 10 K/min to a maximum temperature (T_i), which in turn is successively increased from 473 K to 873 K at 50 K steps. Afterwards, the sample is cooled down to the initial temperature at the same rate.

After each IAC, PALS measurements are carried out at room temperature (RT) using a fast-fast timing coincidence spectrometer of 250 ps resolution at FWHM. H1949-50 Hamamatsu photomultiplier tubes are equipped with BC-442 plastic scintillators and suited in a collinear geometry. A 15μCi ^{22}NaCl positron source covered in Kapton is sandwiched by a pair of identical samples. All spectra have been collected with more than 3×10^6 counts and analyzed with the POSITRONFIT[47] code. The analysis has been performed subtracting the source contribution, which consists in two components. First, a component with a lifetime $\approx$ 1500 ps[48,49] with a measured average intensity of 2.5 %. The second component, with an intensity of $\approx$ 13 %, is related with the positron annihilation in a 7.5 μm width kapton foil that wraps the ^{22}NaCl positron source. The characteristic positron lifetime in Kapton has a very well-known value of 382 ps[50,51]. The obtained χ^2 values has been kept below 1.2 in all fittings.

III. COMPUTATIONAL METHOD

For a better understanding of the experimental results, theoretical calculations of the positron lifetimes have been conducted for the two systems of samples. Using a two component density functional theory[52,53] the annihilation rate λ, (i.e., the inverse of the τ positron lifetime) is evaluated by overlapping the positron density $n_+(\mathbf{r})$ and the electron density of the solid $n_-(\mathbf{r})$ as

$$\lambda = \tau^{-1} = \pi c r_o^2 \int n_+(\mathbf{r}) n_-(\mathbf{r}) \gamma(\mathbf{r}) \mathrm{d}\mathbf{r} \qquad (1)$$

where c is the speed of light in vacuum, r_0 the classical electron radius and $\gamma(\mathbf{r})$ the so-called enhancement factor that comprises the enhanced electron density due to the Coulombic attraction exerted by e^+. The positron lifetime for the perfect (i. e., bulk lifetime) and defected lattice has been calculated by Atomic Superposition Approximation method (AT-SUP)[54], which provides values in good agreement with measured positron lifetimes in metals and in semiconductors[55–58]. The electron density $n_-(\mathbf{r})$ of the crystal and the crystalline Coulomb potential $V_c(\mathbf{r})$ are constructed by adding individual atomic charges $n_-^{at}(|\mathbf{r}-\mathbf{R}_i|)$ and $V^{at}(|\mathbf{r}-\mathbf{R}_i|)$ potentials over the $\mathbf{R}_i$ occupied atomic sites. Finally, the potential felt by the positron $V_+(\mathbf{r})$ is evaluated by adding the positron-electron correlation potential $V_{corr}[n_-(\mathbf{r})]$ to the Coulombic potential so that

$$\begin{aligned} V_+(\mathbf{r}) &= V_c(\mathbf{r}) + V_{corr}\left[n_-(\mathbf{r})\right] \\ &= \sum_i V^{at}\left(|\mathbf{r}-\mathbf{R}_i|\right) \\ &+ V_{corr}\left[\sum_i n_-^{at}(|\mathbf{r}-\mathbf{R}_i|)\right]. \end{aligned} \qquad (2)$$

The enhancement factor of Eq. (1) and the correlation potential of Eq. (2) have been taken into account within the (i) local density approximation (LDA) and (ii) Generalized Gradient Approximation (GGA) framework.

Within the LDA approximation, the $V_{corr}[n_-(\mathbf{r})]$ has been modelled using the interpolation formula proposed by Boronski and Nieminen[59], which is based on the results of Arponen and Pajanne[60]. For $\gamma(\mathbf{r})$ three different parameterizations have been used. First, the expression proposed by Boronski and Nieminen[59] which is based on the many-body calculation by Lantto[61] (labeled as LDA-BN),

$$\begin{aligned} \gamma(\mathbf{r})^{\mathrm{BN}}_{\mathrm{LDA}} &= 1 + 1.23 r_s + 0.8295 r_s^{3/2} \\ &- 1.26 r_s^2 + 0.3286 r_s^{5/2} + \frac{1}{6} r_s^3 \end{aligned} \qquad (3)$$

where $r_s = (3/4\pi n_-)^{1/3}$. The other two expressions suggested by Barbiellini *et al.*[62] are based on results of Arponen and Pajanne[60] and labeled as LDA-AP1

$$\gamma(\mathbf{r})^{\mathrm{AP1}}_{\mathrm{LDA}} = 1 + 1.23r_s - 0.0742r_s^2 + \frac{1}{6}r_s^3 \qquad (4)$$

and LDA-AP2

$$\gamma(\mathbf{r})^{\mathrm{AP2}}_{\mathrm{LDA}} = 1 + 1.23r_s - 0.91657r_s^{3/2} + 1.0564r_s^2 - 0.3455r_s^{5/2} + \frac{1}{6}r_s^3. \qquad (5)$$

Within the GGA approximation, both correlation potential and the enhancement factor have been taken into account using the expression employed by Barbiellini *et al.*[57,62] (based on results of Arponen and Pajanne[60]). Regarding $\gamma(\mathbf{r})_{\mathrm{GGA}}$, it is deduced from the enhancement factor obtained within LDA. The effects of the non-uniform electron density are modeled by a parameter $\epsilon = |\Delta \ln n_-|^2 / q_{TF}^2$ which describes the reduction of the screening cloud close to the positron, being q_{TF} the local Thomas-Fermi screening length. Finally, an adjustable parameter α is also introduced, so the corrected enhancement factor then reads,

$$\gamma(\mathbf{r})_{\mathrm{GGA}} = 1 + (\gamma(\mathbf{r})_{\mathrm{LDA}} - 1)\, e^{-\alpha\epsilon}. \qquad (6)$$

The value of α is set to be $\alpha = 0.22$, which has been proven to give lifetimes for different types of metals and semiconductors in good agreement with experimental results[62]. For GGA calculations, two parameterization for the $\gamma(\mathbf{r})_{\mathrm{GGA}}$ of Eq. (6) has been used: (*i*) the expression of Eq. (4) (labeled as $\gamma(\mathbf{r})^{\mathrm{AP1}}_{\mathrm{GGA}}$) and (*ii*) the expression of Eq. (5) (labeled as $\gamma(\mathbf{r})^{\mathrm{AP2}}_{\mathrm{GGA}}$). It is noteworthy to mention that when $\alpha \to 0$ the Eq. (6) turns into $\gamma(\mathbf{r})_{\mathrm{GGA}} = \gamma(\mathbf{r})_{\mathrm{LDA}}$.

Positron lifetime calculations have been conducted for all Sn_x and In_x samples. Even though the sample $Ni_{50}Mn_{40}In_{10}$ has not been synthesized and experimentally measured by PALS, this composition has been added to the calculations in order to complete the theoretical study. The crystallographic data used in the calculations are shown in Table I. The simulated structure for each sample has been chosen accordingly to the proper phase at RT. Samples without MT and samples with $T_{MT} < RT$ (Sn_{25}, Sn_{20}, In_{25}, In_{20} and Sn_{15}, In_{16}) have been simulated by using the cubic $L2_1$ austenitic structure. Regarding the calculations of the martensitic phase, most of previous works indicate a monoclinic martensite with different degrees of modulation[14,15,24,25]. For the sake of simplicity (specially for vacancy calculations), the martensitic phase have been modeled considering a non-modulated orthorhombic martensite (using the lattice parameters of the monoclinic structure and fixing $\beta = 90^{\mathrm{o}}$), which has been proven to give identical results compared to those obtained considering a monoclinic structure.

The annihilation rate λ of Eq. (1) is evaluated in both Γ and L points in the Brillouin zone, as well as calculating the mean value of the wave functions from Γ and L points. The simulations are performed using the supercell approach. The supercells corresponding to off-stoichiometric samples have been built starting from a stoichiometric lattice and by substituting Sn/In atoms by Mn atoms until matching the proper composition of each sample. The corresponding supercell is increased in size until a convergence of 0.1 ps is reached in bulk lifetime calculations. Afterwards, in order to overcome the artificial defect-defect interactions caused by periodic boundary conditions, the supercell containing vacancy defects is built with increasing size in order to ensure the convergence of 0.1 ps in lifetime calculations and 0.01 eV in positron binding energies.

The maximum number of atoms used in the vacancy calculations has been 500 atoms for the austenitic phase and 512 atoms for the martensitic phase using a $5 \times 5 \times 5$ and $4 \times 4 \times 4$ expansions of the primitive unit cell, respectively. A mesh size of 160^3 points have been used for both phases. Finally, taking into account the potential felt by the positron $V_+(\mathbf{r})$ of Eq. (2) and the enhancement factor $\gamma(\mathbf{r})$, the Schrödinger equation is solved iteratively at the mesh points of the supercell using a numerical relaxation method[63], from which positron wave functions and their energy eigenvalues are obtained to evaluate the λ annihilation rate of Eq. (1).

IV. RESULTS

A. Experimental results

Fig. 1 shows the experimental average positron lifetime ($\overline{\tau}$) values measured for both Sn_x and In_x series as a function of T_i. The first point of PALS measurements corresponds to the AQ $\overline{\tau}$ value. In both set of samples, the AQ state ranges between 181 - 187 ps. The quenching procedure has been repeated more than three times resulting on identical results. In order to study the vacancy dynamics, AQ samples have been subjected to IAC. In both Sn_x and In_x systems, apart from slight fluctuations of 2 - 3 ps, $\overline{\tau}$ remains almost constant regardless the T_i. Only In_{16} and Sn_{15} samples show a significant drop of $\overline{\tau}$. This drop takes place at 773 K and 573 K temperatures respectively, approaching the $\approx$ 178 ps value. However, this drop is rapidly recovered during the next IAC and finally, the $\overline{\tau}$ increases back to its initial AQ's value. The observed moderate evolution of $\overline{\tau}$ can be understood by the physics governing the positron trapping at defects.

When a positron enters a solid, it thermalizes and diffuses through the lattice, until eventually the positron is annihilated with a surrounding electron. In a defect-free lattice, the positron annihilates from the delocalized state (i. e., Bloch state) at an average, λ_b rate or with a characteristic τ_b lifetime (bulk lifetime). However, when open volume defects are present they may act as positron trapping centers. Actually, in the specific case of vacancy defects they act as deep traps for positrons due to the lack of the positive ion. The trapping occurs when a positron

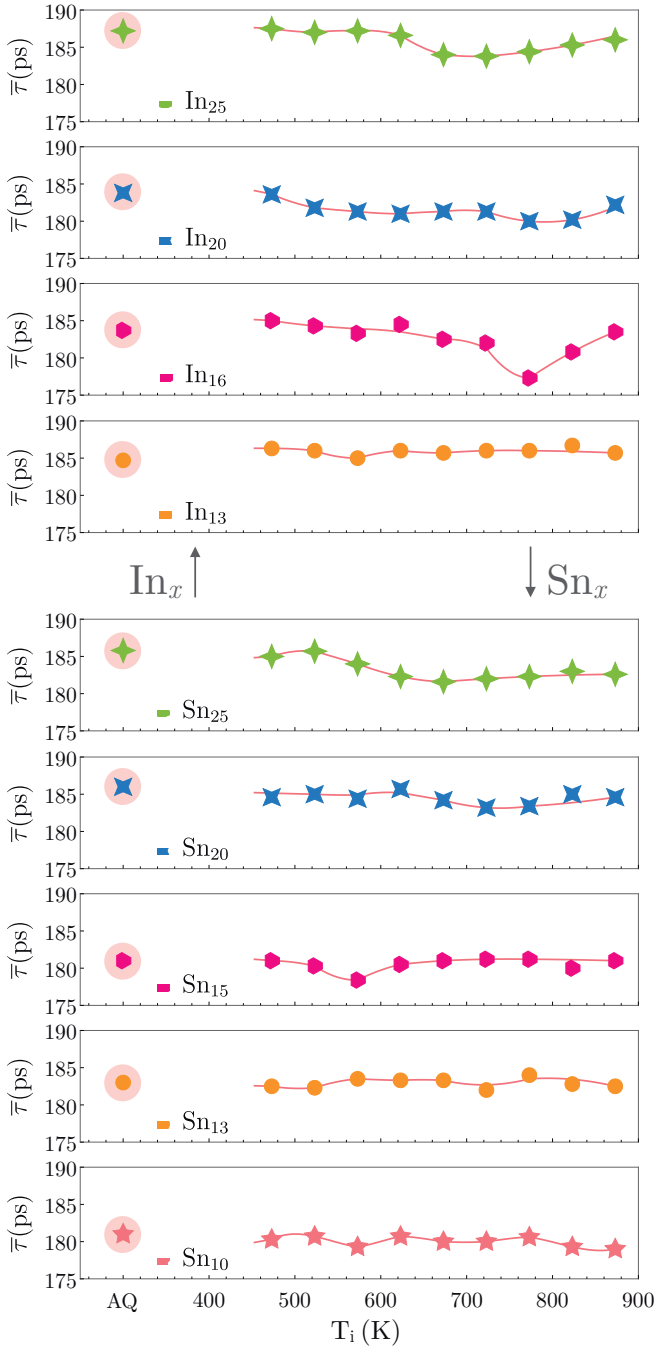

FIG. 1. Experimental average positron lifetime $\overline{\tau}$ values for Sn_x and In_x set of samples. The red-shadowed points correspond to $\overline{\tau}$ values measured in the as-quenched state. The remaining points correspond to $\overline{\tau}$ values as a function of T_i of IAC. The joint line is a guide for the eye. Experimental errors lie within the markers size.

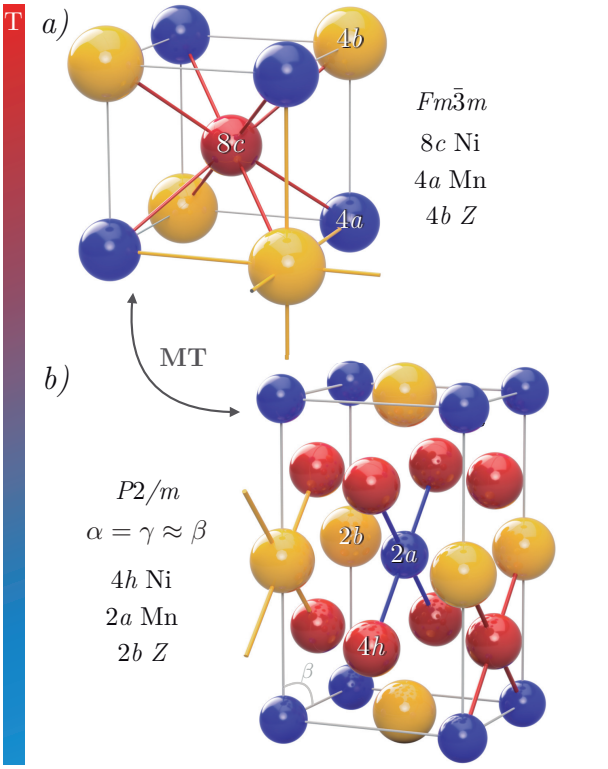

FIG. 2. Schematic representation of stoichiometric (a) high temperature austenite phase and (b) martensite phase. In austenite phase Ni atoms are bound to 4 Mn and 4 Sn/In atoms, whereas Z and Mn atoms are always surrounded by 8 Ni atoms. In the martensite phase, due to the lack of cubic symmetry, Z and Mn atoms are bound to 4 Ni atoms, whereas Ni atoms are bound to 2 Mn and 2 Z atoms. In off-stoichiometric conditions, Mn atoms tend to occupy $4b$ and $2b$ positions.

turns from the Bloch state into a localized state within a vacancy (i.e., the positron wave function becomes localized at the vacancy). The lack of the ion leaves behind an open volume that in turn is characterized by a lower electron density comparing with the perfect lattice.

As it is shown in Eq. (1), the lower the electron density is, the lower is λ. Thus, positrons trapped at vacancies annihilate from a localized state at an average rate $\lambda_v < \lambda_b$, thus exhibiting a longer vacancy-related positron lifetime τ_v, where $\tau_v > \tau_b$.

As a result, the moderate variation of $\overline{\tau}$ shown by Fig. 1 can be explained considering two different scenarios. On the one hand, the lack of open-volume defects (e. g., vacancies) would imply that all positrons only annihilate from the delocalized state or bulk state. Then, the measured lifetime would reflect the lifetime related to the bulk lifetime, τ_b. On the other hand, due to a high C_v retained during the quenching, the contribution of the positrons annihilating from vacancies could become the one dominating $\overline{\tau}$, overcoming the contribution of positrons annihilating from the delocalized state (i. e., bulk). In such scenario, the measured lifetime would reflect the characteristic positron lifetime τ_v related to the present vacancy defect.

Even though the decomposition of the spectra would provide valuable information about different contributions of $\overline{\tau}$, the spectra could not be decomposed in none of Sn_x and In_x samples. As will be discussed fur-

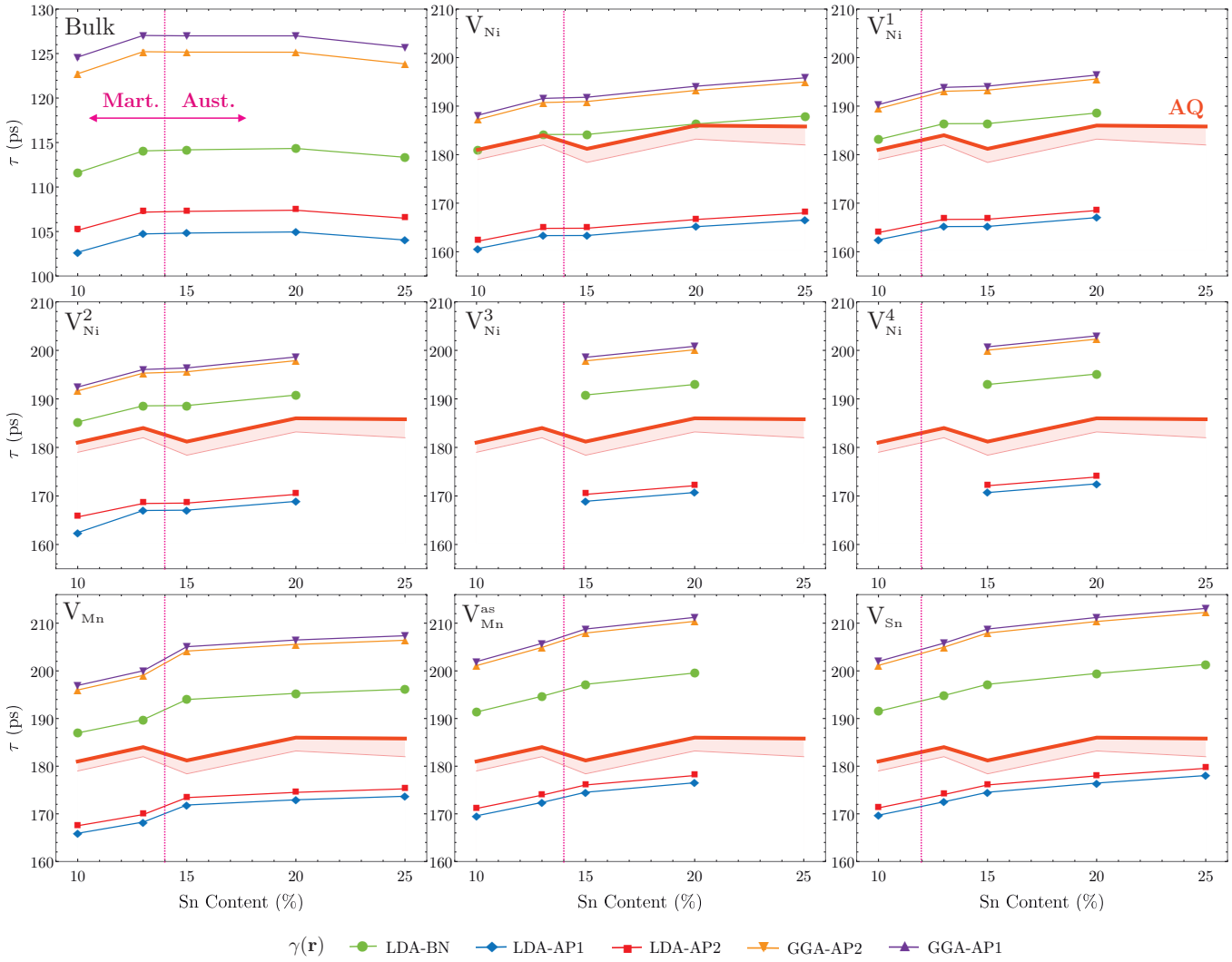

FIG. 3. Theoretical positron lifetimes for $Ni_{50}Mn_{50-x}Sn_x$ ($x = 25, 20, 16, 13, 10$) alloyscalculated for the perfect lattice (bulk) and for each vacancy type defect. The red-shadowed area represents the range of the maximum and the minimum experimental $\overline{\tau}$ values measured after IAC. The upper thick line of the shadowed area represents $\overline{\tau}$ values of samples measured in the AQ state. Theoretical errors lay within the size of markers.

ther in Sec. V, the saturation trapping regime of vacancies hinder the decomposition of the decay spectrum of positrons.. However, $\overline{\tau}$ is the statistically most accurate parameter in PALS experiments, and along with theoretical calculations, it provides information for data interpretation in cases where the experimental data cannot be decomposed[64]. In order to find out whether the measured lifetime is related with the bulk lifetime or with the presence of vacancy defects, experimental results are complemented with theoretical DFT electron-positron calculations.

B. DFT electron-positron results

Theoretical calculations for the bulk and defected lattice for Sn_x and In_x systems have been performed using AT-SUP method. For each sample the simulated structure has been chosen to match the proper phase at RT, see Table I. Besides, calculations for the defected lattice have been taken into account considering several type of posible vacancy defects.

Fig. 2 illustrates the austenitic and martensitic structures, as well as the nearest neighbors (NN) of each type of atom. In the stoichiometric $Fm\bar{3}m$ phase (see Fig. 2a), Ni atoms occupy 8*c* positions, Mn atoms 4*b* positions and *Z* atoms (Ga/Sn/In) atoms 4*a* positions. However, as the Mn content increases on detriment of *Z* atoms, the exceeded Mn atoms tend to occupy 4*b* positions[14,15]. As a result, in off-stoichiometric samples two types of non-equivalent Mn atoms are present. In the studied samples the Ni content has been fixed to 50% and the Mn/*Z* ratio is the one that is modified throughout the studied samples. It is noteworthy to mention that regardless

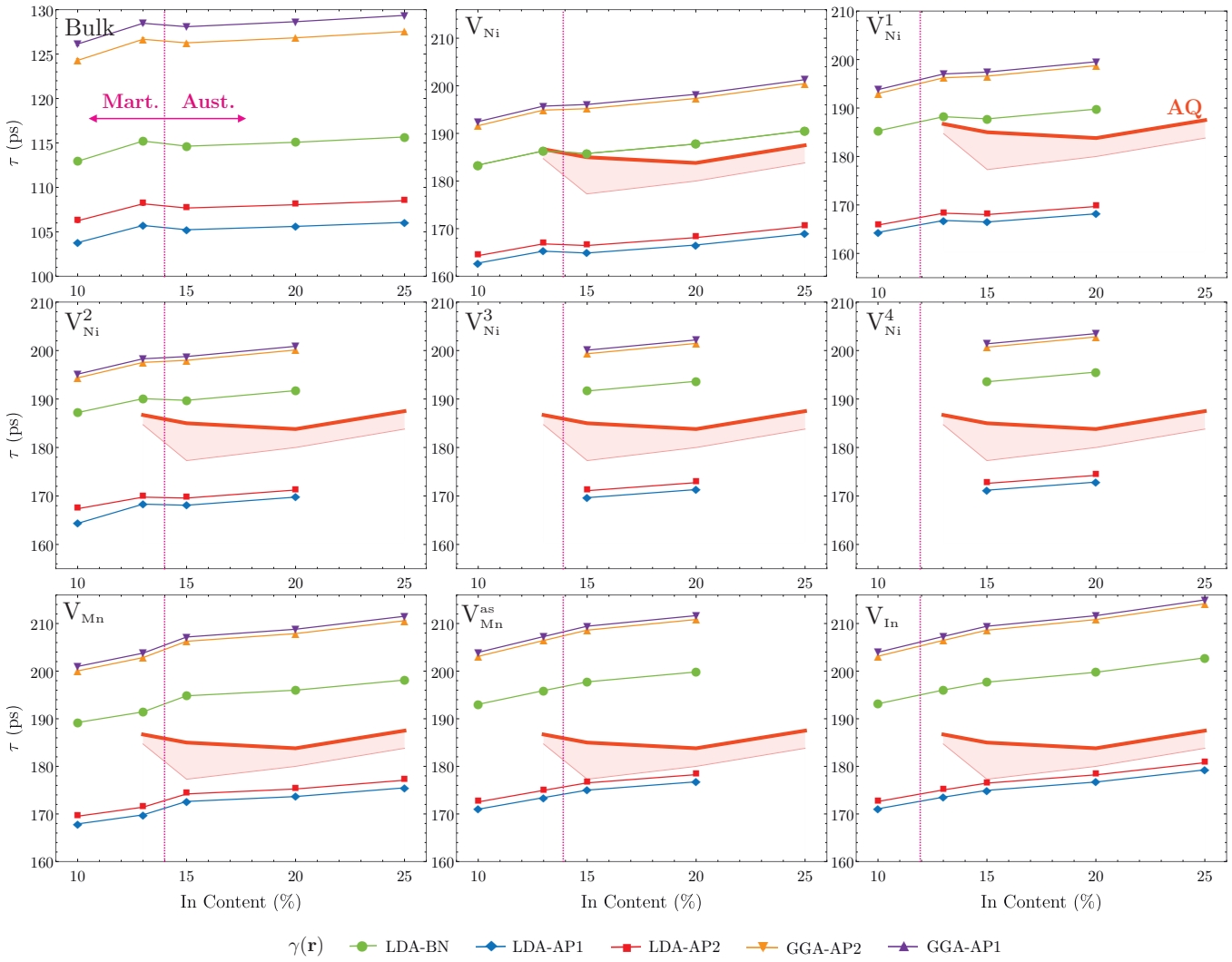

FIG. 4. Theoretical positron lifetimes for $Ni_{50}Mn_{50-x}In_x$ ($x = 25, 20, 16, 13, 10$) alloys calculated for the perfect lattice (bulk) and for each vacancy type defect. The red-shadowed area represents the range of the maximum and the minimum experimental $\overline{\tau}$ values measured after IAC. The upper thick line of the shadowed area represents $\overline{\tau}$ values of samples measured in the AQ state. Theoretical errors lay within the size of markers.

the composition, the NN of both Mn and In/Sn atoms (positions 4*a* and 4*b*) are always Ni in both Sn_x and In_x systems . Regarding the Ni atom, while in stoichiometric conditions the NN of Ni are 4 Mn atoms and 4 *Z* atoms, as soon as the Mn content increases, the probability of Ni atoms to be coordinated with more Mn atoms than *Z* atoms also does. With respect to the possible vacancies present in the studied samples, apart from Ni, Mn and Z vacancies (V_{Ni}, V_{Mn} and V_Z respectively), additional possible vacancies have been also taken into account in off-stoichiometric calculations: V^{as}_{Mn}, which refers to the vacancy of the antisite Mn atom located at 4*b* positions, and V^{i}_{Ni}, which refers to the Ni atoms surrounded for different Mn/Z atoms.

The previous description can be extended to the martensitic structure. However, due to the cell-contraction caused by the MT, and its consequent symmetry breaking, the NN of Ni atoms change. As illustrated in Fig. 2b, in the martensitic structure, contrary to the cubic structure, Ni atoms are not bound to 8 atom but to 4 atoms (i. e., two Mn atoms and two *Z* atoms). As previously pointed out, the exceeded Mn atoms occupy 2*b* positions and the probability of a Ni atom to bound more Mn atoms than *Z* atoms is non-negligible in samples far away from stoichiometry (i. e., Sn_{13}, Sn_{10}, In_{13} and In_{13}).

In summary, for stoichiometric Sn_{25} and In_{25} samples, three different types of possible vacancy defects have been considered: V_{Ni}, V_{Mn} and V_Z. Regarding the off-stoichiometric samples, additional V^{as}_{Mn}, V^{1}_{Ni}, V^{2}_{Ni}, V^{3}_{Ni} and V^{4}_{Ni} vacancies have been also introduced in the calculations. The Ni vacancy surrounded by 4 Mn and 4 *Z* atoms has been labeled as V_{Ni}, while V^{1}_{Ni} refers to the Ni vacancy surrounded by an antisite Mn atom, which

results on a Ni vacancy defect with 5 Mn atoms and 3 Z at NN. Using the same scheme, the remaining type of Ni vacancies are labeled accordingly, and finally, V^4_{Ni} is assigned to the vacancy of a Ni atom surrounded by 8 Mn atoms. For the martensitic phase, V^1_{Ni} and V^2_{Ni} labels have been used to refer to the Ni vacancies with 3 and 4 Mn atoms at NN, respectively.

The results of the calculations are shown in Fig. 3 for Sn_x and in Fig. 4 for In_x. Each figure gathers the calculated positron lifetime (τ) values for perfect and defected lattices. The different outcomes of the five different parameterizations employed for modeling $\gamma(\mathbf{r})$ (described in Sec. III) are plotted comparatively as a function of composition. Additionally, the range of experimental $\overline{\tau}$ is also plotted by a red-shadowed area.

On the one hand, the lifetime values calculated within GGA are higher than the LDA ones. Although $\overline{\tau}$ values predicted by AP1 and AP2 parameterizations are very similar to one another, the absolute values predicted by these two parameterizations within the GGA and LDA approximations are significantly different, separated by $\approx$ 30 ps offset. Otherwise, $\gamma(\mathbf{r})^{BN}_{LDA}$ parameterization give intermediate values of the positron lifetimes comparing with the values calculated by using $\gamma(\mathbf{r})_{GGA}$ (for the two parameterizations) and the two parameterizations $\gamma(\mathbf{r})^{AP1}_{LDA}$ and $\gamma(\mathbf{r})^{AP2}_{LDA}$.

V. DISCUSSION

In order to explain the evolution shown by $\overline{\tau}$ as a function of T_i (see Fig. 1), in Sec. IV A two possible scenario have been proposed. The first scenario, in which due to a lack of open volume defects all positrons are annihilating from the delocalized state at a constant rate $\lambda_b = \tau_b^{-1}$, would imply that $\overline{\tau} \approx \tau_b$. As shown in Fig. 3 and Fig. 4, the calculated bulk lifetime for both systems ranges between 100 - 130 ps. However, experimental $\overline{\tau}$ values range between 177 - 190 ps. Taking into account that the dispersion of theoretical results between the different parameterizations $\gamma(\mathbf{r})$ is $\approx$ 30 ps, experimental $\overline{\tau}$ values are significantly above the calculated bulk lifetimes.

In a second scenario, it is posed that the behaviour of $\overline{\tau}$ may be related with the presence of vacancies. Due to a high C_v retained during quenching, the contribution of the positrons annihilating from vacancies may become the one dominating $\overline{\tau}$, which would overcome the bulk's contribution. In such scenario, $\overline{\tau}$ would approach τ_v. In this connection, theoretically calculated vacancy-related positron lifetimes are more compatible with the experimental results, laying between 170 - 210 ps.

Additionally, the calculated density plots shown in Fig. 5 indicate that the positron density is highly localized within vacancies (i. e., the probability density of the positron is maximum in the vacancy). For the undefected solid the highest position probability density is found at interstitial regions, whereas $|\Psi_+|^2$ vanishes close to atomic nuclei. DFT calculation reveal that regardless the vacancy type, structure and composition, the binding energies of positrons to vacancies range $\approx$ 2-3 eV. Therefore, positron lifetime calculations reveal that the studied vacancies act as effective positron traps. Taking into account that $\overline{\tau}$ values $\approx$ 180 ps reported in Ni-Mn-Ga alloys were ascribed to the presence of vacancies[41–44], it is reasonable to assess that vacancies are present in the studied Sn_x and In_x samples. As a result, the measured $\overline{\tau}$ comprehends two different contributions.

Let's define η_1 as the percentage of total positrons annihilated from the delocalized state with a characteristic lifetime τ_b. Considering the presence of a single vacancy acting as positron trap (or an effective vacancy type accounting the contribution of several vacancy defects with similar τ_v[42]), the rest of positrons (η_2) get trapped at the vacancy and they annihilate from the localized state with a characteristic lifetime τ_v related to the defect. As a result, the experimentally measured $\overline{\tau}$ comprehend these two contributions, so that, $\overline{\tau} = \eta_1\tau_b + \eta_2\tau_v$. Thus, a larger C_v implies a higher probability of positrons annihilating from vacancies. In such scenario, the relation between C_v and $\overline{\tau}$ is given by the so-called *one-trap model*[64],

$$\overline{\tau} = \tau_b \frac{1 + \kappa_v \tau_v}{1 + \kappa_v \tau_b} \tag{7}$$

or,

$$\kappa_v = \mu_v C_v = \frac{1}{\tau_b} \frac{\overline{\tau} - \tau_b}{\tau_v - \overline{\tau}} \quad \rightarrow \quad C_v = \frac{1}{\tau_b \mu_v} \frac{\overline{\tau} - \tau_b}{\tau_v - \overline{\tau}} \tag{8}$$

where κ_v is the so-called trapping rate and is proportional to C_v[66]. The parameter μ_v is the specific trapping coefficient of the vacancy and it depends on the type of defect and also on the surrounding lattice[67]. The trapping rate κ_v describes how effective is a certain type of defect trapping positrons. As shown in Eq. (7) and Eq. (8), a high value of μ_v or C_v would result on a $\overline{\tau}$ value close to τ_v. In metals, unlike in semiconductors, the specific trapping rate μ_v is constant and it does not depend on temperature[67]. In the present work a constant $\mu_v = 1.5 \times 10^{14}$ s^{-1} value has been used, which is widely employed for Ni[68,69].

The lack of variation of experimental $\overline{\tau}$ values reflect that the vacancy contribution to $\overline{\tau}$ remains almost unaltered as a function of the IAC. Additionally $\overline{\tau}$ values are significantly higher than theoretical τ_b values, and indeed, $\overline{\tau}$ values are closer from the calculated vacancy-related lifetimes. All in all, and taking into account the fact that spectra could not be decomposed, the behaviour exhibited by $\overline{\tau}$ as a function of T_i indicates that it lies in a so-called saturation trapping regime. In such regime, $|\overline{\tau} - \tau_v| < 10$ ps[64], due to a high C_v, the contribution of positrons trapped at vacancies dominates $\overline{\tau}$, in such a way that the decomposition becomes unfeasible. Indeed, different fitting procedures have been followed to decompose the spectra without success. It is due to the

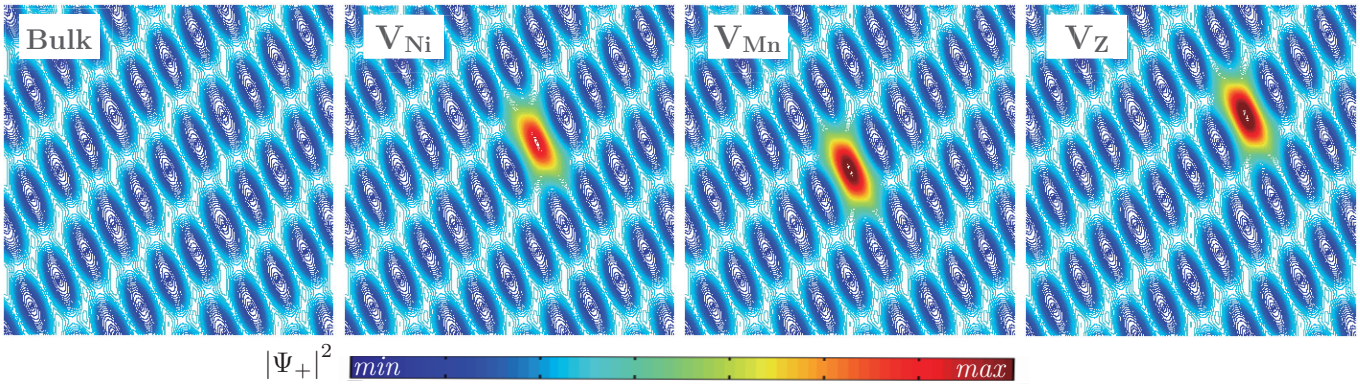

FIG. 5. From left to right, the calculated positron density for a perfect lattice (bulk), and for a defected lattice with V_{Ni}, V_{Mn}, and V_Z, respectively, plane (110). The trapping features exhibited by all samples are identical. The plot is represented in a non-orthogonal symmetric set of primitive vectors for the face-centered cubic lattice[65].

fact that when C_v is high enough, the component related to positron vacancy trapping approaches ≈ 100 %, making very difficult the spectra decomposition. As a result, in PALS spectra only $\overline{\tau}$ can be extracted, which in the saturation trapping regime, $\overline{\tau} \approx \tau_v$. Thereby, $\overline{\tau}$ values corresponding to AQ states are the ones that approach best the characteristic vacancy-related lifetime.

Fig. 3 and Fig. 4 show the overlap of theoretical and experimental $\overline{\tau}$ results (red shadowed area). On the one hand, in both Sn_x and In_x systems, regardless the calculated type of defect, GGA seems to overestimate the positron lifetime. Indeed, in the case of V_{In} and V_{Sn} the predicted lifetimes lie above of 210 ps, 20 ps higher than the experimental $\overline{\tau}$ values, which range between 178 - 190 ps. However, it is noteworthy to mention that this fact alone, does not imply that $\gamma(\mathbf{r})_{\mathrm{GGA}}$ results are not compatible with the experimental results. In principle, according to Eq. (7), a non-saturated regime of vacancies with a higher characteristic lifetime than the measured $\overline{\tau}$ could reproduce a $\tau_v > \overline{\tau} > \tau_b$. However, if the values predicted by $\gamma(\mathbf{r})_{\mathrm{GGA}}$ were accurate, $\overline{\tau}$ would not be in a saturated trapping regime, which would enable the spectra to be decomposed. As previously pointed out the decomposition is not feasible in none of the studied samples, which implies that $\gamma(\mathbf{r})_{\mathrm{GGA}}$ gives overestimated values.

On the other hand, within the LDA framework, both $\gamma(\mathbf{r})^{\mathrm{AP1}}_{\mathrm{LDA}}$ and $\gamma(\mathbf{r})^{\mathrm{AP2}}_{\mathrm{LDA}}$ systematically underestimate the positron lifetime. Because $\overline{\tau}$ must be always $\overline{\tau} \leq \tau_v$ ($\lim_{\kappa_v \to \infty} \overline{\tau} = \tau_v$), the positron lifetime values predicted by $\gamma(\mathbf{r})^{\mathrm{AP1}}_{\mathrm{LDA}}$ and $\gamma(\mathbf{r})^{\mathrm{AP2}}_{\mathrm{LDA}}$ cannot reproduce the experimental $\overline{\tau}$ values. As shown in Fig. 4, only in the case of the In_{15} sample, the characteristic lifetimes calculated by using $\gamma(\mathbf{r})^{\mathrm{AP1}}_{\mathrm{LDA}}$ and $\gamma(\mathbf{r})^{\mathrm{AP2}}_{\mathrm{LDA}}$ for $V^{\mathrm{as}}_{\mathrm{Mn}}$ and V_{In} vacancies approach the experimental lifetimes. However, the calculated $\overline{\tau}$ values do not approach the AQ experimental values (which best approach the defect related characteristic positron lifetimes), but the minimum experimental $\overline{\tau}$ values. As a result, $\gamma(\mathbf{r})^{\mathrm{AP1}}_{\mathrm{LDA}}$ and $\gamma(\mathbf{r})^{\mathrm{AP2}}_{\mathrm{LDA}}$do not predict the appropriate value either.

Phase	Cell parameters		τ
	Atom	Site	$\gamma(\mathbf{r})^{\mathrm{BN}}_{\mathrm{LDA}}$
Austenite Ref. [70]	Ni	8*c* (1/4,1/4,1/4)	182 ps
$Fm\bar{3}m$, 225	Mn	4*a* (0,0,0)	185 ps
$a = 5.8229$ Å	Ga	4*b* (1/2,1/2,1/2)	185 ps
	Bulk		108 ps
Martensite Ref. [71]	Ni	4*d* (0,1/2,1/4)	178 ps
$I4/mmm$, 139	Mn	2*b* (0,0,1/2)	182 ps
$a = b = 3.865$ Å	Ga	2*a* (0,0,0)	181 ps
$c = 6.596$ Å	Bulk		106 ps

Table II. Structural parameters used for theoretical positron lifetime calculations for Ni_2MnGa alloy using $\gamma(\mathbf{r})^{\mathrm{BN}}_{\mathrm{LDA}}$ parameterization. The last column gathers the theoretical vacancy-related positron lifetime of the corresponding atom, along with τ_b bulk lifetime.

Regarding the positron lifetime values calculated by using the $\gamma(\mathbf{r})^{\mathrm{BN}}_{\mathrm{LDA}}$ parameterization, they lie between those predicted within GGA, and the lifetimes predicted by using $\gamma(\mathbf{r})^{\mathrm{AP1}}_{\mathrm{LDA}}$ and $\gamma(\mathbf{r})^{\mathrm{AP2}}_{\mathrm{LDA}}$. In fact, as shown in Fig. 3 and Fig. 4, it seems that the most accurate values comparing the experimental results are given by $\gamma(\mathbf{r})^{\mathrm{BN}}_{\mathrm{LDA}}$ parameterization.

A. Theoretical calculations on Ni_2MnGa

For the sake of validating the accuracy of $\gamma(\mathbf{r})^{\mathrm{BN}}_{\mathrm{LDA}}$ parameterization in Sn_x and In_x systems, positron lifetime calculations have been performed on Ni_2MnGa sample. Taking advantage of the existing PALS results in the literature on Ni_2MnGa[43,44], calculated values have been compared with the available experimental results.

The crystallographic details, along with the results of theoretical positron calculations on Ni_2MnGa are gathered in Table II. Calculations have been carried out for both austenite ($Fm\bar{3}m$)[70] and tetragonal martensite ($I4/mmm$)[71] following the methodology described in Sec. III.

The calculated vacancy-related positron lifetime in Ni_2MnGa ranges between 178 - 184 ps and the lifetime calculated for the martensite phase is ≈ 3-4 ps lower than those calculated in austenite phase. Here, as observed in Sn_x and In_x systems, the calculated vacancy-related positron lifetime of V_{Mn} and V_{Sn} are higher than the one of V_{Ni}. Moreover, either for vacancy-related positron and for bulk lifetimes, the range of the calculated values for Ni_2MnGa matches those calculated for Sn_x and In_x.

The experimental values measured by Merida *et al.* for AQ Ni_2MnGa samples are are around 180 - 182 ps[43,44]. The positron lifetime value related to V_{Ni} in the austenite phase (see Table II) is the one that approaches best the experimental lifetimes measured for AQ Ni_2MnGa samples.. It is important to notice that these experimental values correspond to $\overline{\tau}$ values measured in the austenite phase. The $\overline{\tau}$ value measured in AQ Ni_2MnGa sample was attributed to the presence of an effective vacancy defect, which concentration ranged between 1000 - 2000 ppm. In a nutshell, the present theoretical calculations performed by employing $\gamma(\mathbf{r})^{\mathrm{BN}}_{\mathrm{LDA}}$ parameterization in Ni_2MnGa and the experimental $\overline{\tau}$ values are in a good agreement, which confirms the validity of the calculations by using $\gamma(\mathbf{r})^{\mathrm{BN}}_{\mathrm{LDA}}$. Moreover, the best agreement between experimental $\overline{\tau}$ values and calculated defect-related lifetimes in Sn_x and In_x systems is achieved by using $\gamma(\mathbf{r})^{\mathrm{BN}}_{\mathrm{LDA}}$ parameterization. Thereby, during the rest of the article the results obtained by means of $\gamma(\mathbf{r})^{\mathrm{BN}}_{\mathrm{LDA}}$ will be analyzed.

B. C_v and vacancy-type determination

Theoretical positron lifetimes calculated by using $\gamma(\mathbf{r})^{\mathrm{BN}}_{\mathrm{LDA}}$ parameterizations for Sn_x and In_x systems are listed in Table III. On the one hand, the calculations reveal that both $V^{\mathrm{as}}_{\mathrm{Mn}}$ and V_Z have the same defect-related positron lifetime. As illustrated in Fig. 2, the exceeded Mn atoms tend to occupy the natural positions of Z. Then, Z atoms and antisite Mn atoms are surrounded by the same environment (that is 8 Ni atoms), which results on an identical defect-related positron lifetime. Indeed, the calculated τ values related to V_{Sn} and V_{In} are the largest among the simulated defects, exceeding 200 ps in some In_xsamples. The calculated characteristic lifetimes related to V_{Mn} and $V^{\mathrm{as}}_{\mathrm{Mn}}$ are the next largest, still significantly above from the measured $\overline{\tau}$.

For each composition of both Sn_x and In_x alloys, the lowest calculated lifetimes values are related to V_{Ni}. Besides, this value decreases as decreasing the stoichiometry of the samples, from ≈ 190 ps down to 181 ps. Regarding the lifetimes related to V^i_{Ni}, for a fixed composition, calculations show that as soon as an additional exceeded Mn atom occupies 4*b* position, the characteristic lifetime related to V^i_{Ni} increases in average ≈ 2 ps, see Table III. Due to the fact that Sn and In carry more electrons (valence and core) than Mn atoms, when an exceeded Mn atom occupies a 4*b* position, the electronic density surrounding V^i_{Ni} decreases. According to Eq. (1), a lower electronic density involves a lower annihilation rate λ_v and therefore, a higher defect-related τ_v lifetime.

Z_x	τ_b	V_{Ni}					V_{Mn}		V_Z
		V_{Ni}	V^1_{Ni}	V^2_{Ni}	V^3_{Ni}	V^4_{Ni}	V_{Mn}	$V^{\mathrm{as}}_{\mathrm{Mn}}$	
Sn_{25}	113	187	(–)	(–)	(–)	(–)	196	(–)	201
Sn_{20}	114	186	189	191	193	195	195	200	200
Sn_{15}	114	184	186	189	191	193	194	197	197
Sn_{13}	114	184	186	189	(–)	(–)	190	195	195
Sn_{10}	111	181	183	185	(–)	(–)	187	191	191
In_{25}	116	191	(–)	(–)	(–)	(–)	198	(–)	203
In_{20}	115	188	190	192	194	196	196	200	200
In_{16}	114	186	188	190	192	194	195	198	198
In_{13}	115	186	188	190	(–)	(–)	191	196	196
In_{10}	113	183	185	187	(–)	(–)	189	193	193

Table III. Results of the calculated positron lifetime (in ps) for the perfect lattice, and for several type of vacancy defects in Sn_x and In_x systems, by means of $\gamma(\mathbf{r})^{\mathrm{BN}}_{\mathrm{LDA}}$ parameterization.

Finally, as Fig. 3 and Fig. 4 show, the calculated τ values for V_{Ni} are the ones that present the best agreement with AQ $\overline{\tau}$ values, illustrated in the upper-part of the red-shadowed area. In the Sn_x set, for Sn_{25}, Sn_{20}, Sn_{13} and Sn_{10}, the measured $\overline{\tau}$ value and the predicted values match perfectly, while for Sn_{13} the deviation is ≈ 1 ps. The calculated τ values related to the rest of vacancies are all 4 ps above. In the case of In_x alloys, again, the best accordance between the measured and calculated lifetime is observed for V_{Ni} defect. In the specific case of In_{16} and In_{13} the calculated lifetime matches with the $\overline{\tau}$ experimental value and for In_{20} and In_{25} the deviation is about 2 ps. Thus, in the light of experimental and theoretical results of Sn_x and In_x systems, along with the good agreement between $\gamma(\mathbf{r})^{\mathrm{BN}}_{\mathrm{LDA}}$ outcomes and experimental PALS results in Ni_2MnGa system, it is concluded that V_{Ni} is the vacancy type trapping positrons in Ni-Mn-Sn and Ni-Mn-In alloys.

This experimental result is in agreement with previous theoretical predictions. Recently Wang *et al.*[39] have shown that the most favorable type of defect in Ni-Mn-Ga samples is V_{Ni}. Regarding Ni-Mn-Sn and Ni-Mn-In samples, previous theoretical works also point out to V_{Ni} as the most favorable defect. Reports of Kulkova *et al.*[36,37] show that the formation energy E_f of V_{Ni} is the smallest in both Ni_2MnSn and Ni_2MnIn systems, with $E_f = 0.4$ eV and $E_f = 0.7$ eV values, respectively, whereas the formation energy of V_{Mn} and V_Z are 1.04 eV and 2.59 eV in Ni_2MnSn and 1.58 eV and 2.29 eV in Ni_2MnIn. J. Bai *et al.*[33–35] also suggest V_{Ni} as the most favorable type of

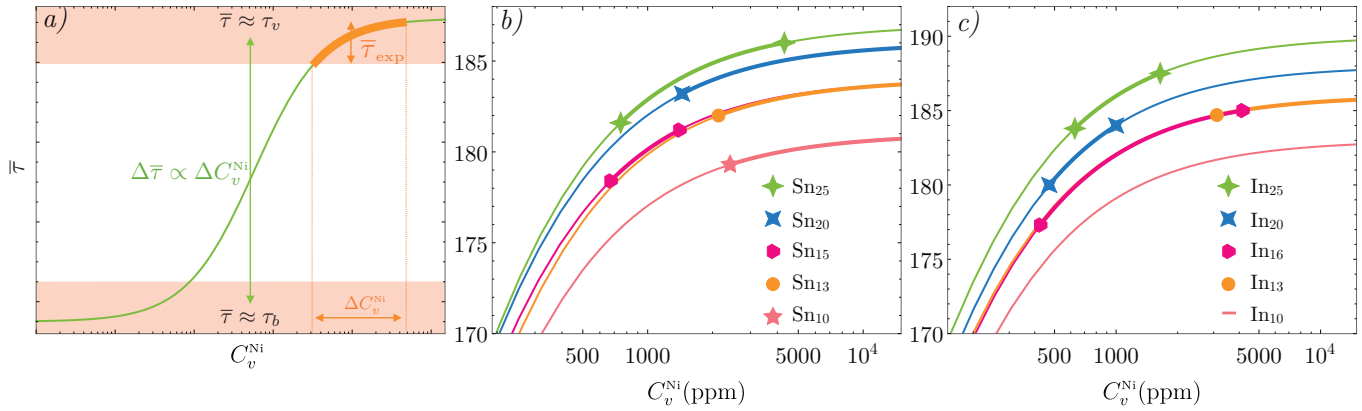

FIG. 6. (a) Positron lifetime sensitivity to the vacancy concentration calculated by Eq. (8). The upper and lower red-shadowed areas correspond to the saturated and diluted vacancy regime, respectively. Calculated evolution of C_v ($\overline{\tau}$) for (b) $Ni_{50}Mn_{50-x}Sn_x$ (x = 25, 20, 15, 13, 10) and (c) $Ni_{50}Mn_{50-x}In_x$ (x = 25, 20, 16, 13, 10) systems derived from Eq. (8) by using theoretical τ_b and τ_v values predicted by $\gamma(\mathbf{r})^{BN}_{LDA}$ of Table III. The markers delimiting the thick lines represent the C_v^{Ni} range calculated from experimental $\overline{\tau}$ values.

defect with E_f = 0.59 eV for in Ni_2MnIn alloy. Thus, taking into account the theoretical predictions, and the experimental and theoretical PALS results of the present work, it is concluded that in Ni-Mn-Ga, Ni-Mn-Sn and Ni-Mn-In systems the present vacancy is V_{Ni}.

The V_{Ni} concentration (C_v^{Ni}) can be estimated by means of Eq. (8). Usually, τ_v and τ_b values can be obtained after decomposing $\overline{\tau}$. However, as discussed before, $\overline{\tau}$ could not be decomposed in any of the samples of Sn_x and of In_x. As an alternative way, and taking into account the good agreement between PALS experiments and DFT calculations, theoretically calculated τ_v and τ_b values of Table III have been used to evaluate Eq. (8). Fig. 6(a) shows the generic relation between C_v and $\overline{\tau}$, according to Eq. (8). In the dilute regime of defects, $\overline{\tau}$ lies close to τ_b, and in this range the variation of C_v does not influence significantly $\overline{\tau}$. However, in the midrange, the sensitivity of PALS is maximum, with a linear dependence between C_v and $\overline{\tau}$. Afterwards, in the saturation trapping regime, the sensitivity decreases again and $\overline{\tau}$ approaches τ_v. As it is illustrated by the thick line in Fig. 6(a), PALS measurements on Sn_x and In_x lie in the saturated regime.

Fig. 6(b) and 6(c) gathers the estimated C_v^{Ni} for Sn_x and In_x systems, respectively. The markers that delimit the thick line in each curve indicate maximum and minimum experimentally obtained $\overline{\tau}$ values, and their corresponding C_v^{Ni}. In both, Sn_x and In_x systems the lowest value of experimentally measured vacancy concentration is $\approx$ 500 ppm. The highest C_v^{Ni} value, on the other hand, may go beyond 10^4 ppm. Particularly, in the case of Sn_x the predicted high C_v^{Ni} is a consequence of the lack of sensitivity of the PALS technique in the saturation trapping regime. However, the lower bound of the calculated C_v^{Ni} lies around hundreds of ppm, a high value comparing with those reported in some Ni-Mn-Ga systems[41,42] (around 10 ppm). Regardless the composition, all samples show saturated trapping features. This result indicates that in contrary to what is observed for Ni-Mn-Ga systems, Ni-Mn-Z (Z = In, Sn) present a high irreducible C_v, which hinders its control by conventional heat-treatments.

These results contrast with the ones obtained by Hedayati *et al.*[32], in which they claim that they were able to tune the T_{MT} as a function of V_{Sn} concentration. It is noteworthy to mention that they do not report any experimental evidence of Sn vacancies. On the one hand, the combination of theoretical and experimental PALS results show that the actual vacancy present in Ni-Mn-Sn systems is V_{Ni}. Additionally, it is demonstrated that Ni-Mn-Sn systems are characterized with a high C_v and that their tuning and control by conventional heat-treatments is not straightforward at all.

Indeed, as shown in Fig. 7, the variation of C_v^{Ni} observed in the present work does not produce any T_{MT} shift in $Ni_{50}Mn_{37}Sn_{13}$ sample, which is one of the samples investigated by Hedayati *et al.* The lack of T_{MT} variation is in agreement with the well-known fact that Ni-Mn-Sn systems exhibit a high stability of the $L2_1$ structure, which precludes the variation of the long-range atomic order and its consequent change on T_{MT}[17]. In the light of present results, the capability of V_{Sn} as a parameter to optimize the T_{MT} seems to be unfeasible in Ni-Mn-Sn systems.

VI. CONCLUSIONS

PALS measurements in $Ni_{50}Mn_{50-x}Sn_x$ (x = 25, 20, 15, 13, 10) and $Ni_{50}Mn_{50-x}In_x$ (x = 25, 20, 16, 13) samples are complemented with DFT electron-positron theoretical calculations. The results confirm that experimentally measured $\overline{\tau}$ values correspond to positrons trapped at

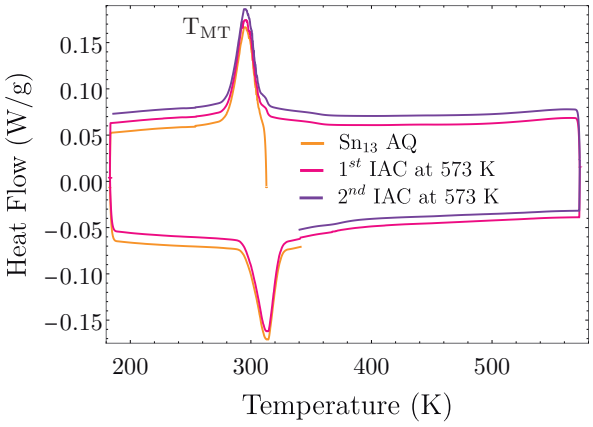

FIG. 7. DSC curves of the AQ Sn_{13} sample, and after two IAC with T_i = 573 K. The T_{MT} remains unchanged even though C_v^{Ni} is different (as revealed by PALS results). Because DSC curves lay at the same position, an offset value has been intentionally added to the IAC DSC curves for a better visualization.

vacancies. In order to establish the parameterization of $\gamma(\mathbf{r})$ which best suits the experimental PALS results, a widely used five different parameterization of $\gamma(\mathbf{r})$ are analyzed within the LDA and GGA schemes, and compared with experimental data. Results indicate that $\gamma(\mathbf{r})^{BN}_{LDA}$ parameterization is the one that best predicts PALS values in the studied systems. Additionally, taking advantage of the existing PALS data in Ni-Mn-Ga systems, the accuracy of $\gamma(\mathbf{r})^{BN}_{LDA}$ parameterization is also tested and confirmed in Ni-Mn-Ga systems. Combining theory and experiments, V_{Ni} is identified as the type of vacancy trapping positrons in Ni-Mn-Z (Z = Ga, Sn, In) samples. The characteristic V_{Ni}-related positron lifetime ranges between 181 - 191 ps. These results show that, unlike what happens in Ni-Mn-Ga alloys, and regardless the the heat-treatments, Ni-Mn-Sn and Ni-Mn-In alloys are characterized by a high C_v^{Ni} ($\geq$ 500 ppm).

VII. ACKNOWLEDGEMENTS

This work is supported by the Basque Government and Spanish Ministry of Economy and Competitiveness under grants IT-1005-16, IT-756-13 and MAT2015-65165-C2-R (MINECO/FEDER). I. Unzueta also wants to acknowledge the Basque Government Grant PRE-2014-214.

* iraultza.unzueta@ehu.eus
† vicente.sanchez@unavarra.es
‡ recarte@unavarra.es
§ ipzlanda@unavarra.es
¶ nerea.zabala@ehu.eus
** joseangel.garcia@ehu.eus
†† fernando.plazaola@ehu.eus

[1] S. Y. Yu, Z. H. Liu, G. D. Liu, J. L. Chen, Z. X. Cao, G. H. Wu, B. Zhang, and X. X. Zhang, Appl. Phys. Lett. **89**, 162503 (2006).
[2] S. Banik, R. Rawat, P. K. Mukhopadhyay, B. L. Ahuja, A. Chakrabarti, P. L. Paulose, S. Singh, A. K. Singh, D. Pandey, and S. R. Barman, Phys. Rev. B **77**, 224417 (2008).
[3] A. Planes, L. Mañosa, and M. Acet, J. Phys. Condens. Matter **21**, 233201 (2009).
[4] L. Mañosa, D. González-Alonso, A. Planes, E. Bonnot, M. Barrio, J.-L. Tamarit, S. Aksoy, and M. Acet, Nat. Mater. **9**, 478 EP (2010).
[5] K. Ullakko, J. K. Huang, C. Kantner, R. C. O'Handley, and V. V. Kokorin, Appl. Phys. Lett. **69**, 1966 (1996).
[6] M. Chmielus, X. X. Zhang, C. Witherspoon, D. C. Dunand, and P. Müllner, Nat. Mater. **8**, 863 EP (2009).
[7] Y. Sutou, Y. Imano, N. Koeda, T. Omori, R. Kainuma, K. Ishida, and K. Oikawa, Appl. Phys. Lett. **85**, 4358 (2004).
[8] P. J. Webster, K. R. A. Ziebeck, S. L. Town, and M. S. Peak, Philos. Mag **49**, 295 (1984).
[9] E. Şaşıoğlu, L. M. Sandratskii, and P. Bruno, Phys. Rev. B **77**, 064417 (2008).
[10] J. M. Barandiarán, V. A. Chernenko, P. Lázpita, J. Gutiérrez, and J. Feuchtwanger, Phys. Rev. B **80**, 104404 (2009).
[11] R. Kainuma, Y. Imano, W. Ito, Y. Sutou, H. Morito, S. Okamoto, O. Kitakami, K. Oikawa, A. Fujita, T. Kanomata, and K. Ishida, Nature **439**, 957 EP (2006).
[12] Z. D. Han, D. H. Wang, C. L. Zhang, H. C. Xuan, B. X. Gu, and Y. W. Du, Appl. Phys. Lett. **90**, 042507 (2007).
[13] T. Krenke, E. Duman, M. Acet, E. F. Wassermann, X. Moya, L. Mañosa, and A. Planes, Nat. Mater **4**, 450 EP (2005).
[14] T. Krenke, M. Acet, E. F. Wassermann, X. Moya, L. Mañosa, and A. Planes, Phys. Rev. B **72**, 014412 (2005).
[15] T. Krenke, M. Acet, E. F. Wassermann, X. Moya, L. Mañosa, and A. Planes, Phys. Rev. B **73**, 174413 (2006).
[16] M. Khan, I. Dubenko, S. Stadler, and N. Ali, J. Phys. Condens. Matter **20**, 235204 (2008).
[17] V. Sánchez-Alarcos, J. Pérez-Landazábal, V. Recarte, I. Lucia, J. Vélez, and J. Rodríguez-Velamazán, Acta Mater. **61**, 4676 (2013).
[18] V. Sánchez-Alarcos, J. López-García, I. Unzueta, J. Pérez-Landazábal, V. Recarte, J. Beato-López, J. García, F. Plazaola, and J. Rodríguez-Velamazán, J. Alloy. Comp **774**, 586 (2019).
[19] V. Sánchez-Alarcos, V. Recarte, J. Pérez-Landazábal, S. Larumbe, R. Caballero-Flores, I. Unzueta, J. García, F. Plazaola, and J. Rodríguez-Velamazán, J. Alloy. Comp **689**, 983 (2016).
[20] I. Unzueta, J. López-García, V. Sánchez-Alarcos, V. Recarte, J. I. Pérez-Landazábal, J. A. Rodríguez-Velamazán, J. S. Garitaonandia, J. A. García, and F. Plazaola, Appl. Phys. Lett. **110**, 181908 (2017).
[21] V. Recarte, J. Pérez-Landazábal, V. Sánchez-Alarcos, and J. Rodríguez-Velamazán, Acta Mater. **60**, 1937 (2012).

[22] A. L. Alves, E. C. Passamani, V. P. Nascimento, A. Y. Takeuchi, and C. Larica, J. Phys. D: Appl. Phys. **43**, 345001 (2010).

[23] A. Ghotbi Varzaneh, P. Kameli, V. R. Zahedi, F. Karimzadeh, and H. Salamati, Metals and Materials International **21**, 758 (2015).

[24] P. J. Brown, A. P. Gandy, K. Ishida, R. Kainuma, T. Kanomata, K.-U. Neumann, K. Oikawa, B. Ouladdiaf, and K. R. A. Ziebeck, J. Phys. Condens. Matter **18**, 2249 (2006).

[25] H. Yan, Y. Zhang, N. Xu, A. Senyshyn, H.-G. Brokmeier, C. Esling, X. Zhao, and L. Zuo, Acta Mater. **88**, 375 (2015).

[26] Y. Zhang, L. Zhang, Q. Zheng, X. Zheng, M. Li, J. Du, and A. Yan, Sci. Rep **5**, 11010 EP (2015).

[27] Z. ni Zhou, L. Yang, J. ge Wang, T. Jin, Y. Huang, J. Li, Q. Hu, and J. guo Li, Prog. Nat. Sci-Mater. **27**, 356 (2017).

[28] S. Kustov, J. Pons, E. Cesari, and J. V. Humbeeck, Acta Mater. **52**, 3075 (2004).

[29] S. Kustov, J. Pons, E. Cesari, and J. V. Humbeeck, Acta Mater. **52**, 3083 (2004).

[30] V. Sánchez-Alarcos, V. Recarte, J. Pérez-Landazábal, and G. Cuello, Acta Mater. **55**, 3883 (2007).

[31] R. Santamarta, E. Cesari, J. Font, J. Muntasell, J. Pons, and J. Dutkiewicz, Scr. Mater. **54**, 1985 (2006).

[32] H. Hedayati, P. Kameli, A. G. Varzaneh, S. Jannati, and H. Salamati, Intermetallics **82**, 14 (2017).

[33] J. Bai, J. M. Raulot, Y. D. Zhang, C. Esling, X. Zhao, and L. Zuo, J. Appl. Phys **108**, 064904 (2010).

[34] J. Bai, N. Xu, J.-M. Raulot, Y. D. Zhang, C. Esling, X. Zhao, and L. Zuo, J. Appl. Phys **113**, 174901 (2013).

[35] J. Bai, N. Xu, J. M. Raulot, C. Esling, X. Zhao, and L. Zuo, Int. J. Quantum Chem **113**, 847 (2012).

[36] S. Kulkova, S. Eremeev, S. Kulkov, and V. Skripnyak, Mat. Sci. Eng. A **481-482**, 209 (2008), proceedings of the 7th European Symposium on Martensitic Transformations, ESOMAT 2006.

[37] S. Kulkova, S. Eremeev, Q. Hu, C. Li, and R. Yang, in *ESOMAT 2009 (Czech Republic, September 7-11, 2009)*, 02017 (EDP Sciences, Les Ulis,France, 2009).

[38] A. Kosogor, V. V. Sokolovskiy, V. A. L'vov, and V. V. Khovaylo, Phys. Status Solidi B **252**, 2309 (2015).

[39] Y. Wang, D. Salas, B. Medasani, P. Entel, I. Karaman, R. Arróyave, and T. C. Duong, Phys. Status Solidi B **255**, 1700523 (2018).

[40] A. Mansouri Tehrani, H. Shahrokhshahi, N. Parvin, and J. Brgoch, J. Appl. Phys. **118**, 014901 (2015).

[41] D. Merida, J. García, V. Sánchez-Alarcos, J. Pérez-Landazábal, V. Recarte, and F. Plazaola, J. Alloy. Comp **639**, 180 (2015).

[42] D. Merida, J. A. García, V. Sánchez-Alarcos, J. I. Pérez-Landazábal, V. Recarte, and F. Plazaola, Appl. Phys. Lett. **104**, 231905 (2014).

[43] D. Merida, J. A. Garíca, E. A. naniz, F. Plazaola, V. Sánchez-Alarcos, J. I. Pérez-Landazábal, and V. Recarte, Physics Procedia **35**, 57 (2012), positron Studies of Defects 2011.

[44] D. Merida, *Caracterización de la Dinámica de Vacantes en Aleaciones Ferromagnéticas con Memoria de Forma del Sistema Ni-Mn-Ga*, Ph.D. thesis, University of the Basque Country (UPV/EHU) (2016).

[45] P. Hautöjarvi, *Positrons in Solids. Topics in Current Physics*, Vol. 12 (Springer, Heidelberg, 1979).

[46] D. Schlagel, R. McCallum, and T. Lograsso, J. Alloy. Comp **463**, 38 (2008).

[47] P. Kirkegaard and M. Eldrup, Comput. Phys. Commun. **7**, 401 (1974).

[48] L. Bertolaccini, M.and Zappa, Il Nuovo Cimento B (1965-1970) **52**, 487 (1967).

[49] B. Somieski, T. Staab, and R. Krause-Rehberg, Nucl. Instrum. Methods Phys. Res., Sect. A **381**, 128 (1996).

[50] K. Plotkowski, T. J. Panek, and J. Kansy, Il Nuovo Cimento D **10**, 933 (1988).

[51] I. K. MacKenzie and J. Fabian, Il Nuovo Cimento B (1971-1996) **58**, 162 (1980).

[52] R. M. Nieminen, E. Boronski, and L. J. Lantto, Phys. Rev. B **32**, 1377 (1985).

[53] E. Boroński and R. M. Nieminen, Phys. Rev. B **34**, 3820 (1986).

[54] M. J. Puska and R. M. Nieminen, J. Phys. F: Met. Phys **13**, 333 (1983).

[55] J. M. C. Robles, E. Ogando, and F. Plazaola, J. Phys.: Condens. Matter **19**, 176222 (2007).

[56] K. O. Jensen, J. Phys.: Condens. Matter **1**, 10595 (1989).

[57] B. Barbiellini, M. J. Puska, T. Korhonen, A. Harju, T. Torsti, and R. M. Nieminen, Phys. Rev. B **53**, 16201 (1996).

[58] T. Korhonen, M. J. Puska, and R. M. Nieminen, Phys. Rev. B **54**, 15016 (1996).

[59] E. Boroński and R. M. Nieminen, Phys. Rev. B **34**, 3820 (1986).

[60] J. Arponen and E. Pajanne, Ann. Physics **121**, 343 (1979).

[61] L. J. Lantto, Phys. Rev. B **36**, 5160 (1987).

[62] B. Barbiellini, M. J. Puska, T. Torsti, and R. M. Nieminen, Phys. Rev. B **51**, 7341 (1995).

[63] G. E. Kimball and G. H. Shortley, Phys. Rev. **45**, 815 (1934).

[64] F. Tuomisto and I. Makkonen, Rev. Mod. Phys. **85**, 1583 (2013).

[65] N. W. ashcroft and N. D. Mermin, *Solid State Physics* (Thomson Learning Inc, 1976).

[66] W. Brandt and R. Paulin, Phys. Rev. B **5**, 2430 (1972).

[67] M. J. Puska and R. M. Nieminen, Rev. Mod. Phys. **66**, 841 (1994).

[68] H.-E. Schaefer, Phys. Status Solidi A **102**, 47 (1987).

[69] T. E. M. Staab, R. Krause-Rehberg, B. Vetter, and B. Kieback, J. Phys.: Condens. Matter **11**, 1807 (1999).

[70] P. J. Brown, J. Crangle, T. Kanomata, M. Matsumoto, K.-U. Neumann, B. Ouladdiaf, and K. R. A. Ziebeck, J. Phys.: Condens. Matter **14**, 10159 (2002).

[71] D. Y. Cong, P. Zetterström, Y. D. Wang, R. Delaplane, R. L. Peng, X. Zhao, and L. Zuo, Appl. Phys. Lett. **87**, 111906 (2005).